**Geomechanics and Engineering**, *Vol. 26, No. 6 (2021) 565-579*
https://doi.org/10.12989/gae.2021.26.6.565


# Experimental and numerical study on strength and deformation behaviors of sandstone with intersecting flaws

Fei Xiong[1,5], Xinrong Liu[*1,2,3], Guangyi Lin[1], Xiaohan Zhou[**1,2,3], Dongshuang Liu[1], Bin Xu[1], Yafeng Han[1], Chunmei He[4] and Zijuan Wang[6]

[1]*School of Civil Engineering, Chongqing University, Chongqing 400045, China*
[2]*State Key Laboratory of Coal Mine Disaster Dynamics and Control, Chongqing University, Chongqing 400044, China*
[3]*National Joint Engineering Research Center of Geohazards Prevention in The Reservoir Areas, Chongqing University, Chongqing 400045, China*
[4]*College of Architectural Engineering, Neijiang Normal University, Neijiang 641100, China*
[5]*State Key Laboratory for Geomechanics and Deep Underground Engineering, China University of Mining and Technology, Xuzhou, Jiangsu 221116, China*
[6]*School of Management Science and Engineering, Chongqing Technology and Business University, Chongqing 400067, China*

*(Received November 20, 2020, Revised July 12, 2021, Accepted September 24, 2021)*

**Abstract.** The distribution pattern of flaws has a significant impact on the mechanical behavior of the rock. To understand the cracking mechanism of the rock with intersecting flaws, the cracking behavior of sandstone containing two intersecting flaws under uniaxial compression was investigated through laboratory tests and particle flow code ($PFC^{2D}$). The strength and failure characteristics of sandstone with intersecting flaws were studied. Subsequently, the evolution of the stress fields and displacement fields were analyzed, and the cracking mechanism of intersecting flaws was discussed. The results showed that the peak stress and average modulus decrease with increasing intersecting angle α of intersecting flaws in both experiments and numerical simulation. The experimental peak stress shows an increasing tendency, while the experimental average modulus first increases and then decreases with increasing direction angle β, which is slightly different from simulation results. The cracking mode of the intersecting flaws was determined by angles α and β. Specifically, when α and β were small, the main fracture surfaces formed at the inner and outer tips of one flaw. When α and β were large, the main fracture surfaces formed at the outer tips of the two flaws. The variation in the high tensile stress zone with α and β is the essential reason for the change in cracking modes with α and β. In addition, a new type of displacement field (defined as DF_IV) related to crack initiation was found. In this type of displacement field, the displacement difference is the main cause of cracking.

**Keywords:** damage evolution; displacement field; intersecting flaws; $PFC^{2D}$; sandstone; stress field

## 1. Introduction

The mechanical behavior of rock mass is largely affected by the presence of discontinuities (Guo *et al.* 2019, Han *et al.* 2020, Wang *et al.* 2019). Under the action of stress, the crack initiates from the tip of the pre-existing flaw. The initiation, propagation, and coalescence of cracks will lead to rock mass failure and instability (Bobet and Einstein 1998, Pizzati *et al.* 2019 and 2020). An in-depth understanding of the fracture evolution of rock is of great significance to the design, construction, and safe operation of rock engineerings such as rock slopes, tunnels, and coal mines (Jing *et al.* 2020, Kou *et al.* 2019, Lv *et al.* 2019, Liu *et al.* 2020).

To explore the fracture mechanism of rock, scholars have conducted many mechanical tests on rock and rock-like materials containing pre-existing flaws, and some primary cracking modes and mechanisms of pre-existing flaws have been obtained. According to the geometric relationship between the new crack and the original crack, the cracks developed from the flaw tip can be classified into wing crack, coplanar crack, and inclined crack (Yang and Jing 2011). Based on the generation mechanism, tensile and shear cracks are generated under tensile and shear stress, respectively. As rock failure is a progressive process, the cracks are generated in a specific order (Lajtai and Jeon 1974, Petit and Barquins 1988). Under uniaxial compression, the tensile crack is generally the first crack formed at pre-existing flaws, followed by the secondary crack. However, the secondary crack may be a tensile crack or shear crack. Generally, flaws usually exist in groups in the actual rock mass. Hence, it is not comprehensive to explore the cracking behavior of a single flaw only.

Based on a single flaw, the cracking behaviors of double flaws (Wong and Li 2013, Tian and Yang 2017), three flaws, and multiple flaws (Sagong and Bobet 2002, Cao *et al.* 2015) in different geometric distributions have attracted much attention. Experimental studies show that two non-parallel flaws are mainly connected by tension cracks or

*Corresponding author, Professor
E-mail: liuxrong@126.com
**Corresponding author, Ph.D.
E-mail: zhouxh2008@126.com



ISSN: 2005-307X (Print), 2092-6219 (Online)

tension-shear cracks under uniaxial compression (Lee and Jeon 2011). The flaw angle and rock bridge angle of two parallel flaws determine the strength and fracture characteristics of the rock-like sample (Zhao *et al.* 2018). Tensile mode, shear mode, and mixed tensile-shear mode are found in the coalescence of two parallel flaws. For samples with three flaws, the peak stress is determined not by the total number of flaws but by the number of flaws that coalesce when rock failure occurs (Wong *et al.* 2001). As for the sample containing multiple flaws, the flaw angle and the number of flaws control the peak strength (Cao *et al.* 2016). Based on the previous experimental studies, the geometric parameters of pre-existing flaws, including flaw angle, length, opening, bridge angle, and bridge length have an important influence on the cracking behavior of rock (Lee and Hong 2018; Manterola *et al.* 2019). However, the previous studies focus mostly on the flaws in intermittent and discrete distribution, and there are few reports on the continuous flaws. In actual rock mass, the distribution of fractures is either discrete or continuous (Yin *et al.* 2016; Liu *et al.* 2019). The study on the cracking mechanism of the continuous crack is not thorough yet.

With the development of computer technology, many numerical simulation methods have been introduced into the study of the deformation and cracking of rock and soil mass, such as the boundary element method (BEM) (Shen 1995), finite element method (FEM) (Carpinteri *et al.* 2008; Yi *et al.* 2021), extended finite element method (XFEM) (Colombo and Massin 2011), discrete element method (DEM) (Scholtès and Donzé 2013; Zhou *et al.* 2021). Among them, the particle flow method (PFC), a method developed based on the discrete element method (DEM), can be used to reproduce the fracture evolution process of rock effectively. When using the bond particle model (BPM), a particular tip-based crack initiation criterion is unnecessary (Potyondy and Cundall 2004; Cho *et al.* 2011). Compared with laboratory tests, numerical simulation is capable and convenient to obtain more information on cracking, such as the stress field and displacement field, which can provide insights into cracking (Camones *et al.* 2013; Zhang and Wong 2014). At present, the particle flow code (PFC) has been widely used in the study of cracking (Jing *et al.* 2021; Lotidis *et al.* 2019; Song *et al.* 2019). For example, Manouchehrian *et al.* (2014) studied the effect of flaw angle on crack propagation behavior of brittle materials such as rock under different compression loads using PFC$^{2D}$. They found that the crack initiation angle became increasingly steeper with the increase of confining pressure. Yang *et al.* (2014) conducted discrete element modeling on coalescence behavior between two unparallel flaws in sandstone under uniaxial compression using PFC$^{2D}$. Cheng *et al.* (2019) conducted numerical simulation on specimens containing en-echelon flaws of various configurations using PFC2D, and results showed that the patterns of linking cracks were dependent on the geometrical arrangement of flaws. To date, particle flow code has become an important method to explore the mechanism of rock cracking. However, the stress field and displacement field information during crack propagation of complex flaws has not been thoroughly analyzed.

For continuous flaws, limited studies have proved that the cracking mechanism of continuous flaws is special, which depends on the geometric features. Sun *et al.* (2019) reported the strength and cracking characteristics of the sample with cross-fractures. They found that peak strength and failure mode are closely related to the horizontal angle, and the fracture length affects the germination and propagation path of the cracks. Zhang *et al.* (2019) experimentally studied the cracking mechanism of a rock-like sample containing two X-type flaws. The results show that flaws tend to coalesce by cracks emanating from flaw tips along a path parallel to the maximum compressive stress direction. Up to now, there are few studies on continuously intersecting flaws that are common in the natural rock mass, and the cracking mechanism of intersecting flaws has not been fully understood.

In this paper, the laboratory tests and discrete element modeling were performed on the sandstone containing two intersecting flaws deformed under uniaxial compression. According to the test results of the intact sample, the microscopic numerical parameters of sandstone were calibrated by the trial and error method. The mechanical response of sandstone with two intersecting flaws under uniaxial compression was simulated systematically and compared with the experimental results quantitatively. Finally, the stress fields and displacement fields during the cracking processes were analyzed through numerical simulation, and the cracking mechanism of two intersecting flaws was discussed.

## 2. Experimental and numerical methodology

### *2.1 Samples with intersecting flaws*

Fig. 1 presents two intersecting flaws (flaws are numbered 1 and 2 clockwise). The length $a$ of each flaw is 20 mm, and the opening is 1.8 mm. The midpoint O of the DE connecting the midpoint of the two flaws is located at the center point of the sample. $\alpha$ is the angle between the two flaws. $\beta$ is the angle between CO and the horizontal direction. In order to study the effects of intersecting angle $\alpha$ and direction angle $\beta$ on the strength and deformation characteristics of sandstone, the angle $\alpha$ increases from 30° to 150° with an interval of 30°, and the angle $\beta$ increases from 0° to 90°, as shown in Table 1. Hereafter, the term "flaw" is employed to describe pre-existing crack, and the term "crack" indicates the newly generated crack or fracture.

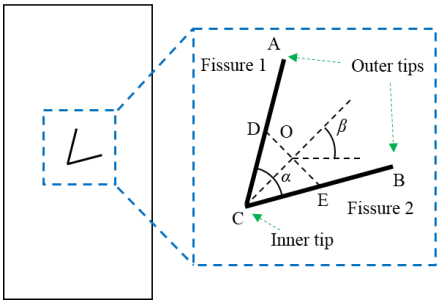


Fig.1. The geometry of intersecting flaws

Table 1 Strength and deformation parameters of sandstone samples containing intersecting flaws (PFC2D simulation)

| Samples | $a$/mm | $\alpha$/(°) | $\beta$/(°) |
|---|---|---|---|
| A01# | 20 | 60 | 0 |
| A02# | 20 | 60 | 30 |
| A03# | 20 | 60 | 45 |
| A04# | 20 | 60 | 60 |
| A05# | 20 | 60 | 90 |
| A06# | 20 | 30 | 45 |
| A07# | 20 | 90 | 45 |
| A08# | 20 | 120 | 45 |
| A09# | 20 | 150 | 45 |

### 2.2 Experimental process

Sandstone materials commonly encountered in the stratum structure were selected as the research objects in the experiment. The sandstone was taken from Linyi City, Shandong Province, China, with a depth of about 18 m and a density of 2441.0 kg/m$^3$. The fresh rock is dark red in the natural state, with uniform particles in size and no visible texture on the surface. The mineral components are mainly quartz and feldspar.

Based on the previous selection of rock sample sizes (Yang *et al.* 2014, Zeng *et al.*), the collected sandstone was cut and polished into rectangular parallelepiped samples with a height, width, and thickness of 160, 80, and 30 mm, respectively. A high-pressure water jet cutting machine was used to prefabricate two intersecting cracks in the sample. During the flaw processing, the water pressure of the high-pressure water jet cutting machine is kept constant to reduce the influence of the change of the flaw opening on the test results. The geometry of the flaw is shown in Fig. 1, and the test of each geometric condition is repeated twice.

The uniaxial compression test of the sandstone sample was carried out on the YNS-2000 electro-hydraulic servo control test system. During the experiment, the displacement load mode was used, and the loading rate was 0.0017 mm/s. Before the test, the petroleum jelly was applied to the upper and lower ends of the sample to reduce the friction effect.

### 2.3 Numerical simulation procedure

#### 2.3.1 Establishment of the numerical model

PFC2D program was selected to study the mechanical behavior of intersecting flaws. In PFC, there are two bond models, one is the contact bond model, and the other is the parallel bond model. The contact bond model can only transfer the force between particles, while the parallel bond model can transfer both force and moment that can better simulate the rock material. Hence the parallel bond model is selected in this paper.

A 2-D numerical model equal to the experimental sample in size (the length is 160 mm, and the width is 80 mm) is established. The particle radius is uniformly distributed in the range of 0.30 to 0.48 mm. Two

Table 2 The micro-parameters used in the PFC2D model for brittle sandstone samples

| Micro-parameters | Values |
|---|---|
| Minimum particle radius $r_{min}$ (mm) | 0.3 |
| Ratio of particle radius $r_{max}$:$r_{min}$ | 1.6 |
| Effective parallel-bond modulus, $\bar{E}_c$ (GPa) | 1.00 |
| Ratio of normal to shear stiffness of the parallel bond, $\bar{k}_n$/ $\bar{k}_s$ | 1.3 |
| Tensile strength of the parallel bond, $\sigma_c$ (MPa) | 14.60 |
| Cohesion of the parallel bond, $c$ (MPa) | 15.80 |
| Friction angle of the parallel bond, $\varphi$ (°) | 46.0 |

Table 3 Comparison between the experimental and numerical mechanical parameters for intact sandstone

| Mechanical parameters of the intact sandstone sample | Experimental values | Simulated values |
|---|---|---|
| Density (kg/m$^3$) | 2441 | 2441 |
| Uniaxial compression strength (MPa) | 86.18 | 87.04 |
| Average modulus (GPa) | 16.93 | 17.13 |

intersecting flaws are established by removing particles from the sample.

A displacement load along the long axial direction is applied on the top of the sample to carry out uniaxial compression. The loading rate is set to 0.05 m/s, which satisfies the static loading condition (Zhang and Wong 2013).

#### 2.3.2 Parameter calibration of numerical simulation

In PFC, the mechanical properties of materials are determined by microscopic parameters. Therefore, it is essential to verify the availability of microscopic parameters. According to the mechanical parameters of intact sandstone samples in laboratory tests (Xiong *et al.* 2017), the microscopic numerical parameters of sandstone are obtained by trial and error. First of all, based on a large number of simulations, the correlation between PFC microscopic parameters and macroscopic mechanical parameters is obtained. The macroscopic parameters are then checked and calibrated by adjusting the microscopic parameters until the numerical sample is consistent with the experimental sample in macroscopic mechanical property. Through the above process, the microscopic numerical parameters which can better characterize the sandstone are gained and shown in Table 2. The comparison of the mechanical parameters between the numerical and experimental samples under uniaxial compression is shown in Table 3, which shows that the two are very close. The comparison of axial stress-strain curves and failure modes between numerical and experimental intact samples is shown in Fig. 2. From Fig. 2(a), except the initial compaction stage, the numerical and experimental stress-strain curves are consistent, and both show prominent brittleness characteristics. It can be seen from Fig. 2(b) that the split failure contributes to the final failure mode of the numerical and experimental sample, and the main fracture

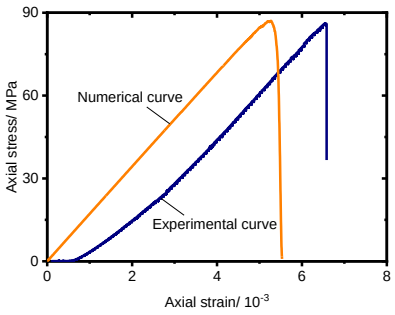


(a) The axial stress-strain curves

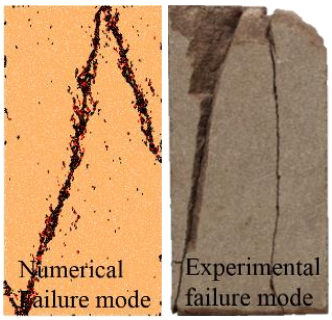


(b) Final failure modes

Fig. 2 Comparison between experimental and numerical results of intact sandstone samples under uniaxial compression.

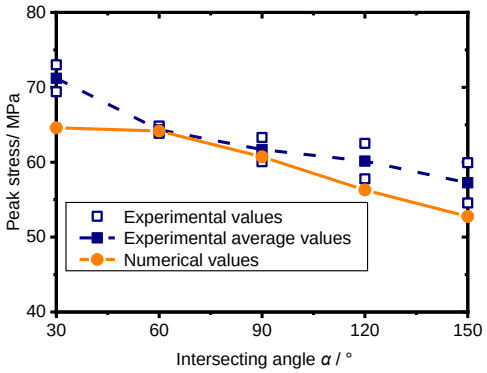


(a) Different $\alpha$

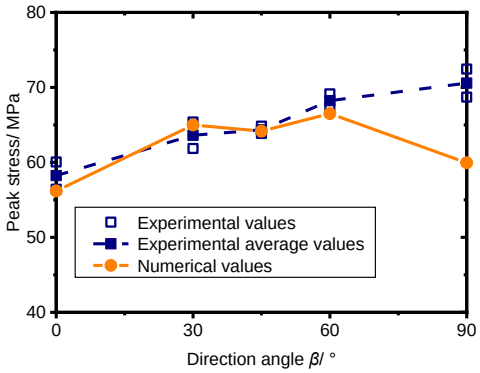


(b) Different $\beta$

Fig. 3 Comparison between experimental and numerical peak stress of sandstone samples containing intersect flaws under uniaxial compression

surface is roughly along the axial direction. The comparisons in Table 3 and Fig. 2 indicate that the PFC microscopic parameters obtained in this paper are reasonable and can be used to study the mechanical and fracture evolution characteristics of sandstone with intersecting flaws under uniaxial compression.

## 3. Mechanical and failure characteristics of sandstone containing intersecting flaws

In this section, the experimental and numerical simulation results are presented and compared with each other to analyze the strength and failure characteristics of sandstone with intersecting flaws. Some of the experimental results utilized for comparison are from the reference (Xiong *et al.* 2017).

### *3.1 Strength and deformation characteristics*

Fig. 3 shows the comparisons between simulated and experimental peak stress with different $\alpha$ and $\beta$. It can be seen from the figure that with the increase of angle $\alpha$, the variations in simulated and experimental peak stress are highly consistent, and both decrease gradually (Fig. 3(a)). Obviously, with the increase of intersecting angle $\alpha$, the flaws span increases so that the effective bearing area of the sample decreases, reducing the bearing strength of the sample.

When $\beta$ increases from 0 to 60°, the experimental and simulated peak stress both increase and are approximately equal to each other for the same $\beta$, as shown in Fig. 3(b). As the direction angle $\beta$ increases, the triangular rock column between the two flaws can bear more force, so the strength of the sample increases. However, as $\beta$ increases to 90°, there is a difference between simulated and experimental peak stress. The experimental peak stress reaches its maximum, while the simulated peak stress decrease. The simulated peak stress is lower by 15.06 % than the experimental average peak stress at $\beta$ of 90°. The difference at $\beta$ = 90° may lie in the heterogeneity of the rock sample and the representativeness of the micro-parameters.

Fig. 4 gives comparisons between simulated and experimental average modulus. As shown in Fig. 4(a), the simulated and experimental average modulus is approximately equal to each other for the same $\alpha$ and both decrease with the increase of angle $\alpha$. The variation is similar to that of peak stress. From Fig. 4(b), one can see that the simulated average modulus is higher by 14.15% than the average experimental value at $\beta$ of 0°, while the simulated average modulus is almost equal to the experimental average modulus for the same $\beta$ when $\beta$ at the range of 30 to 90°. The difference in average modulus at $\beta$ = 0° may be due to different failure modes between numerical simulation and experiment, which is present in section 3.2.

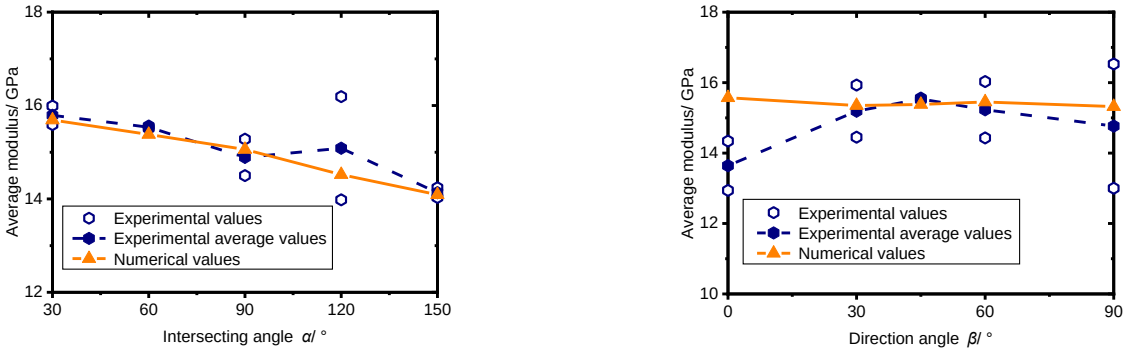


(a) Different $\alpha$ (b) Different $\beta$

Fig. 4 Comparison between experimental and numerical average modulus of sandstone samples containing intersecting flaws under uniaxial compression.

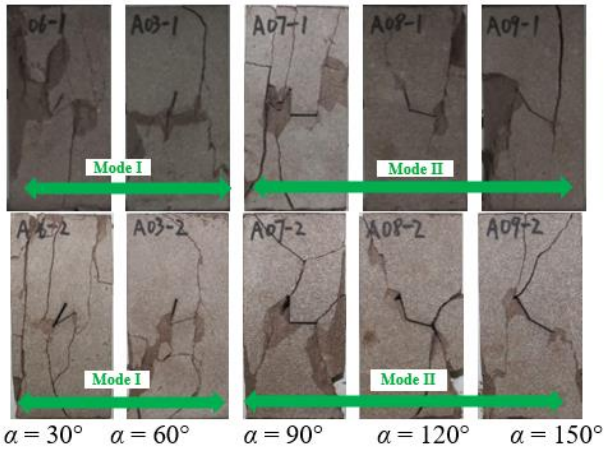


(a) Two groups of experimental results

(b) The numerical results.

Fig. 5 Comparison between experimental and numerical failure mode of sandstone samples containing intersect flaws versu different $\alpha$ with $\beta = 45°$ under uniaxial compression

### *3.2 Final failure modes*

According to the positions of the main fracture surface, three failure modes appear in the sandstone with intersecting fractures under uniaxial compression:

Mode I: the main fracture surfaces are formed at the inner tip and outer tip of flaw 2.

Mode II: the main fracture surfaces are formed at the outer tips of the two flaws.

Mode III: the main fracture surfaces are formed at the inner tip and outer tip of flaw 1.

The final failure mode of sandstone samples containing intersecting flaws is significantly affected by $\alpha$ and $\beta$. The final failure modes with different $\alpha$ under uniaxial compression are shown in Fig. 5. One can see that the failure mode I appear in both numerical and experimental samples at α = 30 and 60°, and the failure mode II appears in the samples with $\alpha$ at the range of 90 ~ 150° regardless of simulated and experimental results. It is clear that the formation positions of the main fracture surfaces change from the inner tip and the outer tip of one flaw to the outer tips of two flaws with the increase of $\alpha$, and the simulated results are highly consistent with the experimental results. This phenomenon indicates that with the increase of $\alpha$, the stress concentration effect at the inner tip decreases, and the stress concentration effect at the outer tip of flaw 1 gradually increases.

The simulated and experimental failure modes of sandstone samples containing two intersecting flaws with

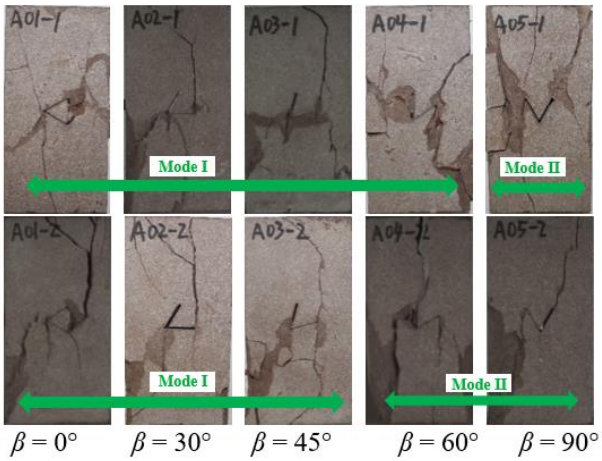


(a) Two groups of experimental results

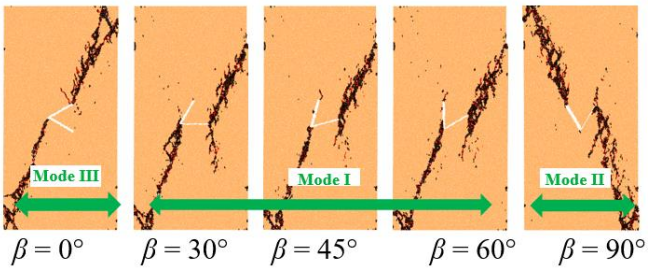


(b) The numerical results.

Fig. 6 Comparison between experimental and numerical failure modes of sandstone samples containing intersecting flaws versus different $\beta$ with $\alpha = 60°$ under uniaxial compression.

different $\beta$ are shown in Fig. 6. From the figure, the failure mode I is related to the first group of experimental samples with $\beta$ in the range of 0 ~ 60° and the second group of experimental samples with $\beta$ in the range of 0 ~ 45° and the numerical samples with $\beta$ in the range of 30 ~ 60°. The failure mode II is related to the first group experimental sample with $\beta$ = 90°, and the second group experimental samples with $\beta$ in the range of 60 ~ 90° and numerical sample with $\beta = 90°$. While the failure mode III applies only to the numerical sample with $\beta = 0°$.

With increasing $\beta$ values, the experimental and simulated failure modes follow the same variation trend, i.e., the formation positions of the main fracture surfaces change from the inner tip and the outer tip of one flaw to the outer tips of the two flaws. The change in the failure modes also implies the change of stress concentration effect at the flaw tip with $\beta$. However, a new failure mode, which was not found in laboratory tests, appears in the numerical sample with $\beta$ = 0°. This difference may result in the experimental average modulus being lower than the simulated average modulus at $\beta$ of 0°, as shown in Fig. 4(b). The difference in failure mode probably lies in that the 2-D model cannot accurately simulate a 3-D experimental sample (Lee and Jeon 2011, Zeng *et al.* 2018).

## 4. Analysis of the cracking process of specimens through stress fields

Stress fields can be employed to explore the cracking mechanism of intersecting flaws. It is difficult to be obtained from laboratory tests but it is much easier in numerical simulation. Therefore, this section studies the stress fields before and after crack initiation through the force chain information recorded by PFC$^{2D}$.

### *4.1 Stress fields before crack initiation*

The crack initiation form reflects the dominant position of cracking. In PFC, macro cracks are formed by a certain number of microcracks. Therefore, it is considered that the crack initiation occurs when the number of microcracks reaches 1.0-2.0% of the number of total cracks in the final failure.

Fig. 7(a) gives the crack initiation forms with different intersecting angles $\alpha$ and the corresponding axial stress (crack initiation stress). It can be seen that with increasing angle $\alpha$, the crack initiation positions changes from the inner tip and outer tip of one flaw to the outer tips of two flaws, and the positions of crack initiation are completely consistent with that of main fracture surfaces for the same $\alpha$. In general, the crack initiation stress decreases with the increase of $\alpha$.

Crack initiation forms of numerical samples containing intersecting flaws with different direction angle $\beta$ are given in Fig. 7(b). When $\beta$ = 0°, the crack is first initiated at the inner tip of the two flaws; When $\beta$ = 30° and 45°, cracks are initiated at the inner tip and the outer tip of flaw 2. When $\beta$ is in the range of 60-90°, cracks are initiated at the outer tips of two flaws. The variation of crack initiation form with different $\beta$ is similar to that of failure mode. There is no

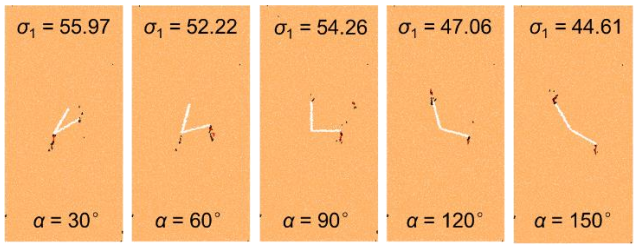


(a) Crack initiation forms with different $\alpha$

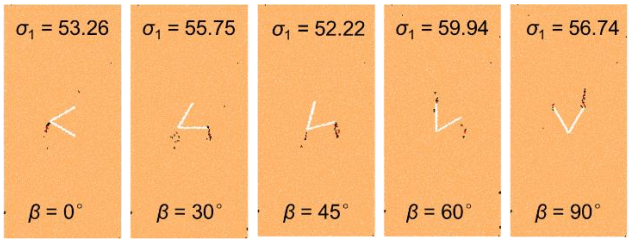


(b) Crack initiation forms with different $\beta$

Fig. 7 Crack initiation forms of numerical samples with different $\alpha$ and $\beta$. The corresponding crack initiation stress (units:MPa) is listed in each image

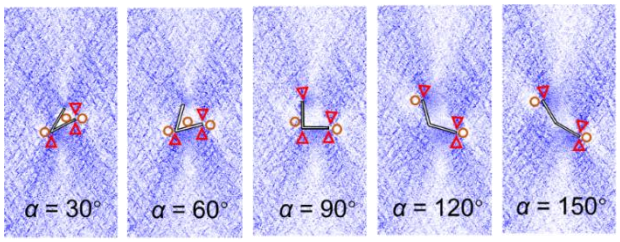


(a) Tensile bond force represented by short blue lines

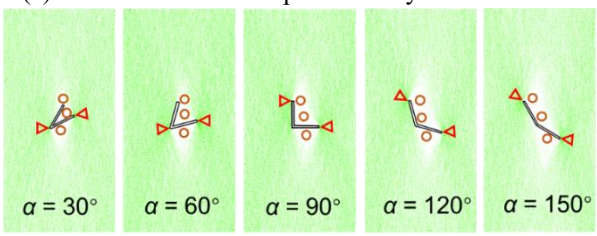


(b) Compressive bond force represented by short green lines

Fig. 8 Global force vector of numerical samples with different $\alpha$ before crack initiation. △: High-stress zone ○: Blank-stress zone

obvious variation law between crack initiation stress and angle $\beta$.

#### *4.1.1 Stress fields before crack initiation with different α*

The stress fields just before crack initiation with different $\alpha$ are given in Fig. 8. The tensile and compressive force fields are analyzed separately. The bonding force is represented by the discrete line segment. The thickness and the direction of the line segment reflect the magnitude and direction of force, respectively. Crack evolution is often related to high stress. The blank-stress zone shows some dependency with different geometries of flaws, so the variations of the high-stress zone and the blank-stress zone with different $\alpha$ and $\beta$ are analyzed in detail below.

Fig. 8(a) shows the variation of the global tensile force vector with different intersecting angles $\alpha$ just before crack initiation. As can be seen from the figure, the high-stress zone of the tensile force is distributed above or below the flaw tip. Additionally, it is distributed radially along the loading direction or at a certain angle to the loading direction, and the stress gradually decreases along the radiation direction. The blank-stress zone is distributed on the left or right of the flaw tip and also formed in the triangular region between the two flaws. The high-stress zone and the blank-stress zone exist almost simultaneously around the flaw tip. The variation in the high-stress zone and the blank-stress zone with $\alpha$ are as follows:

The high-stress zone: With the increase of $\alpha$, the stress within the high-stress zone at the inner tip of the two flaws gradually decreases, and the high-stress zone gradually changes into the low-stress zone. The stress at the outer tip of flaw 1 increases gradually with the increase of $\alpha$ until the high-stress zone appears. The high-stress zone always exists at the outer tip of flaw 2 with different $\alpha$. Combined with the crack initiation form in Fig. 7, one can see that the cracks are formed at the high-stress zone, and the change of the high-stress zone of tensile force with $\alpha$ is similar to that of the crack initiation position of intersecting flaws.

The blank-stress zone: With the increase of $\alpha$, the blank-stress zone in the triangular region between the two flaws and the region near the inner tip disappears gradually. The blank-stress zone appears gradually near the tip of flaw 1 with the increase of $\alpha$. The outer tip of flaw 2 is accompanied by the blank-stress zone for all $\alpha$.

Fig. 8(b) shows the variation of the global compressive force vector of samples with different $\alpha$ before crack initiation. By the figure, it can be seen that the high-stress zone of the compressive force field is also distributed at the left or right of the flaw tip, i.e., it shares the same position with the blank-stress zone of the tensile force around the flaw tip. Hence, with the increase of $\alpha$, the variation of the high-stress zone of the compressive force field is similar to that of the blank-stress zone of tensile force near the flaw tip. The blank-stress zones of compressive force completely wrap two flaws for all $\alpha$, and its axial and horizontal sizes increase slightly with the increase of $\alpha$.

From the above analysis, it is seen that $\alpha$ determines the stress distribution at the flaw tip. In detail, with the increase of $\alpha$, the tensile stress concentration effect at the inner tip of the flaw decreases, but it strengthens gradually at the outer tip of flaw 1. However, the tensile stress concentration zone always exists at the outer tip of flaw 2. Cracks are generated in the high-stress zone of tensile force. Therefore, α changes the cracking pattern by affecting the distribution of the tensile stress concentration zone.

#### *4.1.2 Stress fields before crack initiation with different β*

Fig. 9(a) shows the variation of the tensile force field with different $\beta$ just before crack initiation. From the figure, the changes of the high-stress zone and blank-stress zone of the tensile force field with $\beta$ increasing are obtained as follows.

The high-stress zone: As $\beta$ increases from 0 to 90°, the high-stress zone at the inner tip gradually disappears, eventually evolving into a low-stress zone. When $\beta$ = 0°, the

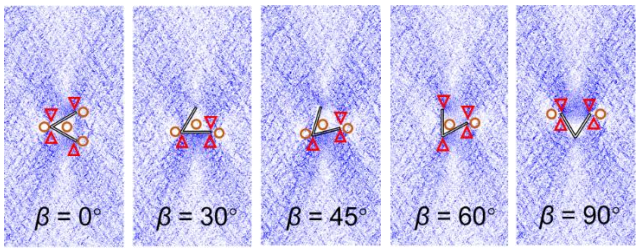


(a) Tensile bond force represented by short blue lines

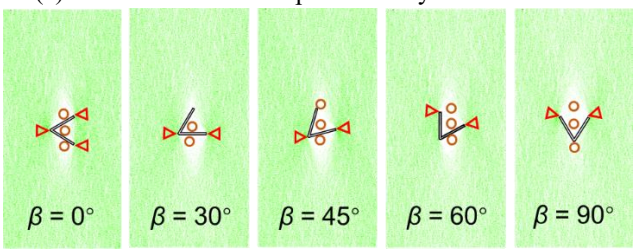


(b) Compressive bond force represented by short green lines

Fig. 9 Global force vector of numerical samples with different $\beta$ before crack initiation. △: High-stress zone ○: Blank-stress zone

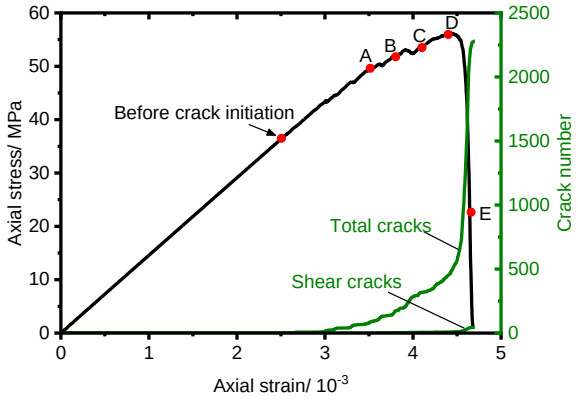


(a) Axial stress-strain curve

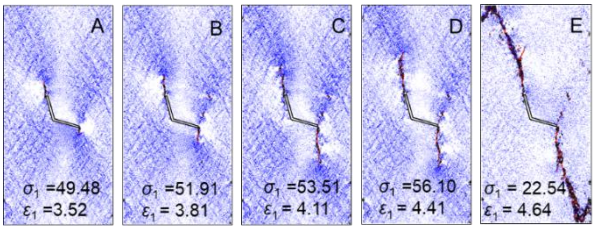


(b) Global tensile force vectors. The corresponding stress (units: MPa) and strain (units: $\times 10^{-3}$) are also given

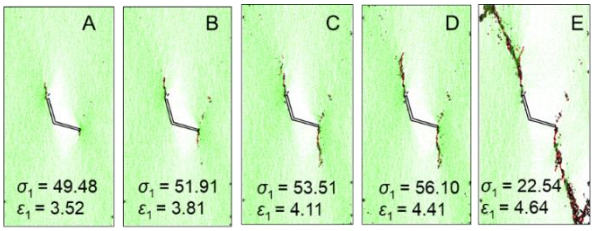


(c) Global compressive force vectors. The corresponding stress (units: MPa) and strain (units: $\times 10^{-3}$) are also given

Fig. 10 Evolution of stress field during crack propagation of sample with $\alpha$=120°, $\beta$=45°

high-stress zone can be seen at the outer tip of flaw 1. However, when $\beta$ is 30°, the outer tip of flaw 1 is in a low-stress zone, and when $\beta$ increases from 30 to 90°, a high-stress zone is gradually formed at the outer tip of flaw 1. There is always a high-stress zone at the outer tip of flaw 2 for all $\beta$. Combined with the crack initiation form in Fig. 7, it can also be found that the cracks are formed at the high-stress zone, and the change of the high-stress zone of tensile force with $\beta$ is similar to that of the crack initiation position of intersecting flaws.

The blank-stress zone: With the increase of $\beta$, the area of the blank-stress zone within the region between two intersecting flaws decreases. The blank-stress zone at the inner tip gradually disappears as $\beta$ increases from 0 to 90°. For the outer tip of flaw 1, the blank-stress zone appears at $\beta$ of 0 and 90°, but disappears when $\beta$ values are in the range of 30 to 60°. The outer tip of flaw 2 is always accompanied by a blank-stress zone for all $\beta$.

Fig. 9(b) shows the global compressive force vector of samples with different direction angle $\beta$ before crack initiation. Also, the variation of the high-stress zone of the compressive force field is similar to that of the blank-stress zone of tensile force near the flaw tip due to the fact that they share the same position around the flaw tip. The blank-stress zone always wraps around two flaws too.

From the above analysis, it can be seen that the stress distribution at the flaw tip is determined by $\beta$, thereby changing the cracking pattern of intersecting flaws.

### *4.2 Crack propagation process*

After carack initiation, the stress field is constantly

adjusted with crack propagation. Taking the sample $\alpha$ = 120° and $\beta$ = 45° as an example, Fig. 10 illustrates the relationship among axial stress-strain curve, crack propagation, and force field distribution during the loading. The capital letters in Fig. 10(a) correspond to the crack evolution process in Fig. 10(b) and (c), and the cumulative curves of numbers of total microcracks and shear microcracks are also presented.

Fig. 11(a) demonstrates that when the microcracks begin to accumulate, the stress curve enters the nonlinear section from the linear elastic segment, and the stress shows fluctuation and drops. Few shear microcracks are generated in the loading process, and the tensile microcracks contribute to the main failure of the sample. From Fig 10. (b), the crack propagates in the radiation area of the high-stress zone of tensile force. The cracks are initiated at the tensile stress concentration position (the high-stress zone of the tensile force). After crack initiation, the high tensile stress at the flaw tip dissipates, and the tensile stress concentration position is adjusted to the new crack tip. The new crack continues to propagate under the action of high tensile stress. Fig. 10(c) shows the change in the compressive force field during loading. It can be seen from the figure that the blank-stress zone of the compressive force field gradually becomes larger with the crack propagation, which is due to the adjustment of compressive force. Bobet (2000) found that after the initiation of the first crack, the singularity of the compressive stress at the tip of the pre-existing flaw would not disappear, which is also found in the present study. Besides, the higher compressive force is also distributed along the crack propagation path until the complete failure of the sample, as shown in Fig. 10(c). Similar laws can be observed in other cases, which will not be described in detail here.

## 5. Evolution of displacement fields under the compression

The displacement field is another important information about crack evolution. This section analyzes the evolution characteristics of the displacement field during the cracking process of intersecting flaws in sandstone.

### *5.1 Introduction of displacement field types*

Zhang and Wong (2012, 2014) have systematically studied the displacement field of rock samples with a single flaw and two parallel flaws under uniaxial compression through PFC$^{2D}$. Three types of displacement fields, namely DF_1, DF_2, and DF_3, associated with the crack propagation, were observed and defined in their studies, as shown in Fig.11. Among them, DF_1 corresponds dominantly to tensile displacement, DF_2 corresponds dominantly to mix tensile-shear displacement, and DF_3 corresponds dominantly to shear displacement. In their study, the uniaxial compression was conducted by applying two opposite displacements on the top and bottom of the sample, respectively. In the present study, a downward displacement load is applied on the top of the sample, while

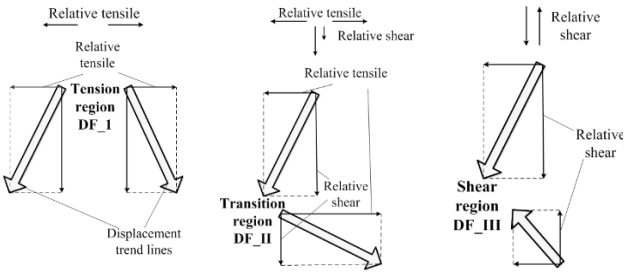


(a) Type I (b) Type II (c) Type III

Fig. 11 Three displacement field types proposed by Zhang and Wong (2012, 2014)

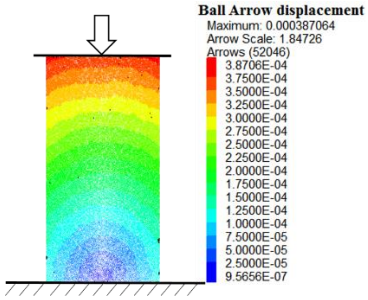


Fig. 12 The global displacement field (with the unit of m) of the intact numerical sample as the load up to $\sigma_1$=78.04 MPa

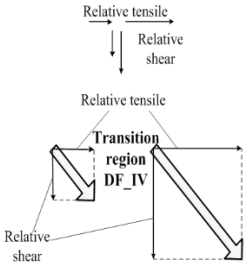


Fig. 13 Type IV displacement field type (DF_IV) defined by displacement trend lines in this paper

the bottom end of the sample is fixed, as shown in Fig. 12, which shows the displacement field of the numerical intact sample when the axial stress is loaded to 78.04 MPa. It is found that the displacement in the upper part of the sample is larger than that in the lower part under unidirectional loading. The displacement isogradient line is convex, and the curvature of the isogradient line at the lower part of the sample is more significant than that in the upper part of the sample. Due to the different loading modes and the geometry of flaws, a new type of displacement field involved displacement difference is observed in the present study, which is defined as DF_IV, as shown in Fig. 13. From the figure, the motion directions of the two displacement trend lines (represented by open arrows) are the same, but the relative shear displacement and relative tensile displacement occur in the concerned areas due to the displacement difference.

### *5.2 Displacement field during crack propagation*

Based on the displacement field classification, this

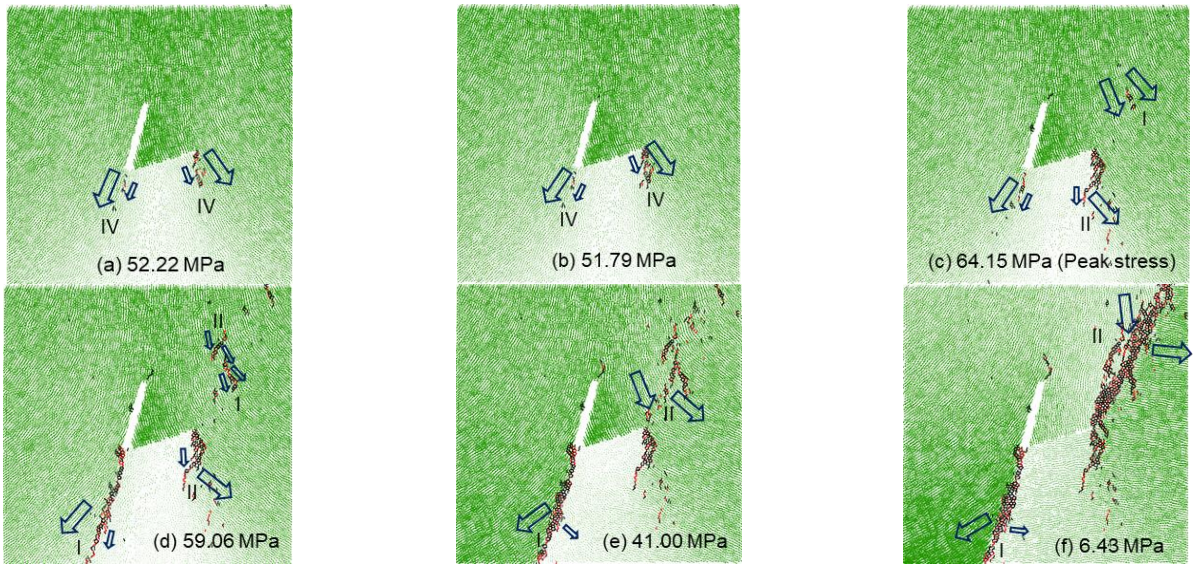


Fig. 14 Displacement vectors (solid green arrows) and displacement trend lines (blue open arrows) around intersecting flaws with $\alpha = 60°$ and $\beta = 45°$ during crack evolution. The corresponding axial stress is given

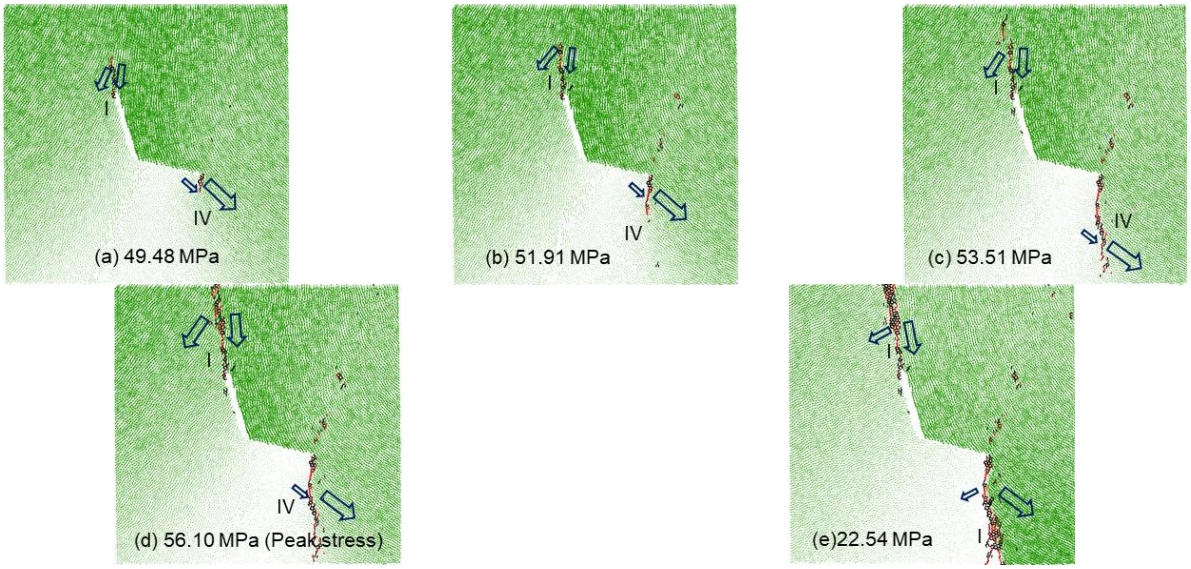


Fig. 15 Displacement vectors (solid green arrows) and displacement trend lines (blue open arrows) around intersecting flaws with $\alpha = 120°$ and $\beta = 45°$ during crack evolution. The corresponding axial stress is given

section focuses on the displacement field related to the cracking process of intersecting flaws. Four typical samples, i.e., sample with $\alpha = 60°$ and $\beta = 45°$, sample with $\alpha = 120°$ and $\beta = 45°$, sample with $\alpha = 60°$ and $\beta = 0°$ and sample with $\alpha = 60°$ and $\beta = 90°$ are demonstrated in Figs. 14-17, respectively. In the figures, micro-tensile cracks and micro-shear cracks are shown in black and red, respectively. The particle displacements are represented by solid green arrows, among which the thick and long arrow indicates a larger particle displacement while the thin and short one indicates a smaller particle displacement. The blue open arrows are employed to indicate the displacement field trend adjacent to the new cracks. If the particle displacement values on two sides of the new crack are quite different, the big and smaller blue open arrows are used to illuminate the larger and smaller displacement, respectively.

#### *5.2.1 Sample with α = 60° and β = 45°*

As the stress reaches 52.22 MPa, two downward propagating cracks are initiated at the inner tip and the outer tip of flaw 2. The displacement trend lines of the two cracks are both parallel, and the displacement differences are significant, so they belong to the type IV displacement field (DF_IV) and are labeled as “IV” in Fig. 14(a). After crack initiation, the stress slightly drops to 51.79 MPa (Fig. 14(b)), and the displacement trend lines of two cracks keep in type IV. As the stress rise to the peak of 64.15 MPa, the displacement trend lines of the crack initiated at the outer tip of flaw 2 are transformed into the type II displacement field (DF_II), and the crack has stopped propagating (Fig. 14 (c)). Meanwhile, a far-field crack is formed, which is related to the type I displacement field (DF_I) at the upper right of the outer tip of flaw 2. After the peak, the stress

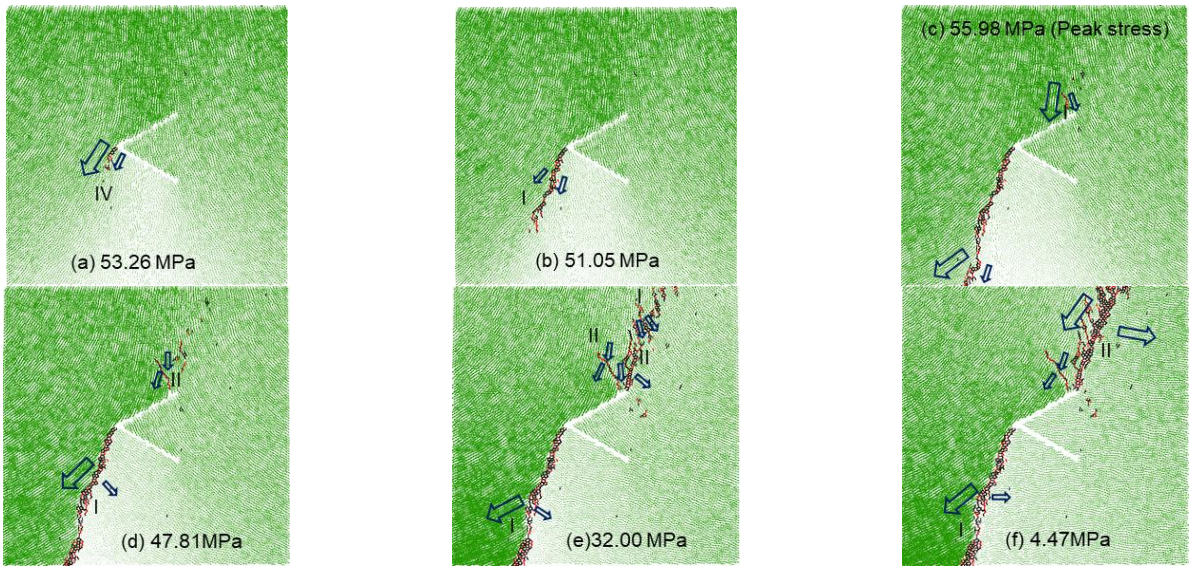


Fig. 16 Displacement vectors (solid green arrows) and displacement trend lines (blue open arrows) around intersecting flaws with $\alpha = 60°$ and $\beta = 0°$ during crack evolution. The corresponding axial stress is given

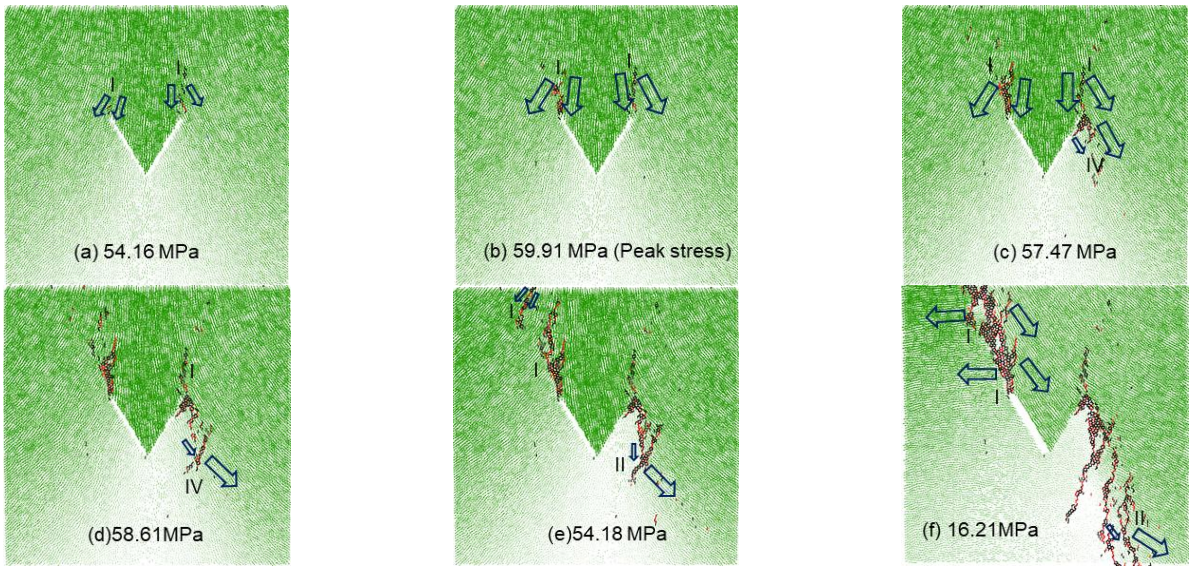


Fig. 17 Displacement vectors (solid green arrows) and displacement trend lines (blue open arrows) around intersecting flaws with $\alpha = 60°$ and $\beta = 90°$ during crack evolution. The corresponding axial stress is given

drops significantly, and the crack initiated from the inner tip propagates continuously and forms a main fracture surface. The displacement field type of this crack evolves from DF_IV to DF_I, as shown in Fig. 14(d)-14(f). Due to displacement difference, the main fracture surface related to the type I displacement field includes micro-shear cracks (shown in red). Another main fracture surface is formed through the coalescence of far-field cracks generated at the upper right of the outer tip of flaw 2. The far-field cracks are initially formed as en-echelon cracks associated with type I and type II displacement fields, as shown in Fig. 14(c) and 14(d). However, when the en-echelon cracks coalesce with each other and form the main fracture surface connecting with the outer tip of flaw 2, the displacement trend lines of this main fracture surface are fixed as type II as shown in Fig. 14(f).

#### *5.2.2 Sample with α = 120° and β = 45°*

The displacement field evolution associated with crack propagation of sample with $\alpha = 120°$ and $\beta = 45°$ is illustrated in Fig. 15. It can be seen from the figure that two cracks generated - one is initiated at the outer tip of flaw 1 associated with type I displacement field, and one is initiated at the outer tip of flaw 2 accomplished by type IV (Fig. 15(a)). These two cracks both propagated continually and formed the main fracture surfaces (Fig. 15(b)-15(e)). It should be noted that the displacement field type of crack generated at the outer tip of flaw 2 finally changed from type IV to I as the main fracture surface is formed.

#### *5.2.3 Sample with α = 60° and β = 0°*

As the stress is loaded to 53.26 MPa, a downward propagating crack is initiated at the inner tip, accompanied

by two parallel displacement trend lines with a large displacement difference. Hence it belongs to the type IV displacement field. However, with the continuous propagation of the crack until the main fracture surface is formed, the corresponding displacement trend lines gradually diverge from each other and evolve from DF_IV to DF_I (Fig. 16(b)-16(f)).

When the stress reaches the peak of 55.98 MPa, as shown in Fig. 16(c), a wing crack accomplished by DF_I is initiated at the outer tip of flaw 1, which includes micro-shear cracks due to displacement difference. The wing crack did not fully expand, and the corresponding displacement field is later transformed into DF_II, as shown in Fig. 16(d)-(f). At the post-peak, when the stress drops to 32.00 MPa (Fig. 16(e)), an upward propagating secondary crack associated with DF_II initiate at the outer tip of flaw 1, and a lot of en-echelon cracks associated with type I form near the outer tip of flaw 1. The secondary crack and en-echelon cracks coalesce with each other and form the main fracture surface, which belongs to type II, as shown in Fig. 16(f).

#### *5.2.4 Sample with α = 60° and β = 90°*

Firstly, two upward propagating cracks are generated at the outer tips of two flaws. They are both related to the type I displacement field, as shown in Fig. 17(a) and 17(b). At a post-peak of 57.47 MPa, a downward propagating crack related to the type IV displacement field is generated at the outer tip of flaw 2. When the stress drops to 54.18 MPa (Fig. 17(e)), a far-field crack associated with type I is formed at the upper left of flaw 1. Meanwhile, the displacement trend lines of downward propagating crack at the outer tip of flaw 2 evolve from DF_IV to DF_II. When the stress further drops to 16.21 MPa, far-field cracks at the upper left of flaw 1 coalesce with the crack initiated from the outer tip of flaw 1 and form the main fracture surface related to the type I displacement field, as shown in Fig.17(f). Simultaneously, several en-echelon cracks are formed at the lower right of the outer tip of flaw 2 and coalesce with the crack from the flaw tip and eventually form another main fracture surface. This main fracture surface is associated with the type II displacement field.

## 6. Discussion

### *6.1 Influence of angles of intersecting flaws on the stress fields and cracking process*

According to the experimental and numerical results, the distribution of stress fields of samples and the cracking forms of intersecting flaws are closely related to the intersecting angle $\alpha$ and direction angle $\beta$. Given that the cracking forms and stress fields of the sandstone samples, the following findings can be made:

Before the crack initiation, the high tensile stress zone is often accompanied by a blank-stress zone of the tensile force around the flaw tip. The blank stress zone of the tensile force and the high-stress zone of compressive force share the same position near the flaw tip. The high-stress zone and the blank-stress zone at the flaw tip can be transformed with each other with varying intersecting angle $\alpha$ and direction angle $\beta$ due to the changes in the mechanical structure. Based on the crack initiation forms plotted in Fig.7, the crack initiation occurs within the high-stress zone of the tensile force. With varying angles $\alpha$ and $\beta$, the position of the high tensile stress zone changes, which is the essential reason for the change of cracking mode. The high-stress zone of the tensile force is the potential mechanism of cracking for the flaw tip.

In addition, when $\alpha$ and $\beta$ are small, there exists a blank tensile and compressive stress zone within the triangular region between the two intersecting flaws, indicating that this region is not subjected to any force. With the increase of $\alpha$ and $\beta$, the area of this region decreases gradually.

During the crack propagation stage, the crack propagates follows the traction of the high-stress zone of the tensile force. In this stage, the high tensile stress at the flaw tip dissipates, and the tensile stress concentration position is adjusted to the new crack tip. The new crack continues to propagate under the action of high tensile stress. The blank stress zone of the compressive force field expands gradually with the crack propagation due to the adjustment of compressive force. The singularity of the compressive stress at the tip of the pre-existing flaw would not disappear. Besides, a higher compressive force is also distributed along the crack propagation path until the complete failure of the sample.

### *6.2 Influence of angles of intersecting flaws on the displacement fields related to cracking process*

From the variation of the displacement fields during the cracking process of sandstone samples, the influences of angles of intersecting flaws on the displacement fields are as follows:

With the increase of $\alpha$ and $\beta$, the initiation displacement field along with the upwardly expanding crack changes from type II to type I. This phenomenon is mainly caused by the reduction of the angle between cracking flaws and the maximum principal stress direction, which promotes the tensile failure of the flaw tip. Besides, the downwardly propagating cracks are initially accompanied by a type IV displacement field. If the downwardly expanding crack continuously expands and forms the main fracture surface, the corresponding displacement field will transform into an I-type displacement field. When the en-echelon cracks are initially formed, the corresponding displacement fields belong to type I or II. However, if the en-echelon cracks coalesce with the cracks accomplished by the type II or IV displacement field and form the main fracture surface, the corresponding displacement field will be transformed into the type II displacement field.

In the present study, the macro cracks related to the type I displacement field contain micro-shear failure due to the presence of displacement differences between two sides of cracks. Type III displacement field is not found in the samples containing intersecting flaws under uniaxial compression. After that, in the process of crack propagation, in addition to the type of displacement field, the displacement difference between the two sides of the crack should also be paid attention to, which plays an important role in cracking. The type of displacement field related to

the cracking is affected by both the loading mode and the geometrical parameters of the pre-existing flaws, so the research on the displacement field still needs further exploration.

## 7. Conclusions

The strength and failure characteristics of sandstone containing two intersecting flaws are investigated through laboratory tests and discrete element simulation. The force field distribution and displacement field evolution during the cracking process are further analyzed by numerical simulation. The following conclusions can be drawn.

• The numerical peak stress and average modulus decrease gradually with the increase of $\alpha$, precisely the same as the experimental results. With the increase of angle $\beta$, the experimental peak stress shows a tendency to increases, while the experimental average modulus first increases and then decreases, reaching the maximum value at $\beta = 45°$. The variation of the numerical peak stress and average modulus with $\beta$ is slightly different from the experimental results, but the difference is reasonable. The cracking modes of intersecting flaws are largely determined by angles $\alpha$ and $\beta$, which are proved by laboratory tests and numerical simulation. With the increase of $\alpha$ and $\beta$, the cracking position of intersecting flaws changes from the inner tip and the outer tip of one flaw to the outer tips of two flaws.

• Through the analysis of the force field, the high-stress zone (stress concentration zone), the low-stress zone, and the blank-stress zone (there is tiny stress in the zone) in the tensile and compressive force field near the intersecting flaws are observed. The change of the high-stress zone of tensile force with $\alpha$ and $\beta$ is the essential reason for the variation of cracking modes of intersecting flaws. The high-stress zone and blank-stress zone of tensile force often exist together near the flaw tip. The blank-stress zone of the tensile force and the high-stress zone of compressive force exist in the same region near the flaw tip. When $\alpha$ and $\beta$ are small, there exists a blank-stress zone of tensile and compressive force within the triangular region between the two intersecting flaws.

• In addition to the three types of displacement fields proposed by previous literature, a new type of parallel displacement field (defined as DF_IV), which is only related to crack initiation, is found. In this type of displacement field, the displacement difference leads to cracking. The upwardly propagating cracks are initially accompanied by the type I or II displacement field that depends on $\alpha$ and $\beta$. While downward propagating cracks are initially associated with type IV. Regardless of whether the crack grows upward or downward, if it continuously expands and forms the main fracture surface, the corresponding displacement field will be transformed into the type-I displacement field.

## Acknowledgments

This work was supported by the National Key R&D Program of China (Grant No. 2018YFC1504802), the National Natural Science Foundation of China (Grant No. 41972266), the Graduate Research and Innovation Foundation of Chongqing, China (Grant No. CYS21029) and Basic Research and Frontier Exploration Project of Chongqing in 2018 (Grant No. cstc2018jcyjAX0453).

## Conflict of interest

The authors declare that there is no conflict of interest regarding the publication of this paper.

## References

Bobet, A. and Einstein, H.H. (1998), "Fracture coalescence in rock-type materials under uniaxial and biaxial compression", *Int. J. Rock Mech. Min. Sci.*, **35**(7), 863-888. https://doi.org/10.1016/S0148-9062(98)00005-9.

Bobet, A. (2000), "The initiation of secondary cracks in compression", *Eng. Fract. Mech.*, **66**(2), 187-219. https://doi.org/10.1016/S0013-7944(00)00009-6

Cao, R.H., Cao, P., Lin, H., Pu, C.Z. and Ou, K. (2016), "Mechanical behavior of brittle rock-like specimens with pre-existing flaws under uniaxial loading: Experimental studies and particle mechanics approach", *Rock Mech. Rock Eng.*, **49**(3), 763-783. https://doi.org/10.1007/s00603-015-0779-x.

Cho, N., Martin, C.D. and Sego, D.C. (2007), "A clumped particle model for rock", *Int. J. Rock Mech. Min. Sci.*, **44**(7), 997-1010. https://doi.org/10.1016/j.ijrmms.2007.02.002.

Cao, P., Liu, T.Y., Pu, C.Z. and Lin, H. (2015), "Crack propagation and coalescence of brittle rock-like specimens with pre-existing cracks in compression", *Eng. Geol.*, **187**, 113-121. https://doi.org/10.1016/j.enggeo.2014.12.010.

Colombo, D. and Massin, P. (2011), "Fast and robust level set update for 3D non-planar X-FEM crack propagation modeling", *Comput. Meth. Appl. Mech. Eng.*, **200**(25-28), 2160-2180. https://doi.org/10.1016/j.cma.2011.03.014.

Cheng, Y., Jiao, Y.Y. and Tan, F. (2019), "Numerical and experimental study on the cracking behavior of marble with en-echelon flaws", *Rock Mech. Rock Eng.*, **52**(11), 4319-4338. https://doi.org/10.1007/s00603-019-01849-x.

Carpinteri, A., Spagnoli, A., Vantadori, S. and Viappiani, D. (2008), "Influence of the crack morphology on the fatigue crack growth rate: A continuously-kinked crack model based on fractals", *Eng. Fract. Mech.*, **75**(3), 579-589. https://doi.org/10.1016/j.engfracmech.2007.05.007.

Camones, L.A.M., Vargas, E.D., de Figueiredo, R.P. and Velloso, R.Q. (2013), "Application of the discrete element method for modeling of rock crack propagation and coalescence in the step-path failure mechanism", *Eng. Geol.*, **153**(2), 80-94. https://doi.org/10.1016/j.enggeo.2012.11.013.

Guo, Q.Z., Su, H.J., Liu, J.W., Yin, Q., Jing, H.W. and Yu, L.Y. (2019), "An experimental study on the fracture behaviors of marble specimens subjected to high temperature treatment", *Eng. Fract. Mech.*, **225**, 106862. https://doi.org/10.1016/j.engfracmech.2019.106862.

Han, G.S., Jing, H.W., Jiang, Y.J., Liu, R.C. and Wu, J.Y. (2020), "Effect of cyclic loading on the shear behaviours of both unfilled and infilled rough rock joints under constant normal stiffness conditions", *Rock Mech. Rock Eng.*, **53**, 31-57. https://doi.org/10.1007/s00603-019-01866-w.

Ingraffea, A.R. and Heuze, F.E. (1980), "Finite element models for rock fracture mechanics", *Int. J. Numer. Anal. Meth. Geomech.*,

**4**(1), 25-43. https://doi.org/10.1002/nag.1610040103.
Jing, H.W., Wu, J.Y., Yin, Q. and Wang, K. (2020), "Deformation and failure characteristics of anchorage structure of surrounding rock in deep roadway", *Int. J. Min. Sci. Technol.*, **30**(5), 593-604. https://doi.org/10.1016/j.ijmst.2020.06.003.
Jing, H.W., Yin, Q., Yang, S.Q. and Chen, W.Q. (2021), "Micro-mesoscopic creep damage evolution and failure mechanism of sandy mudstone", *Int. J. Geomech.*, **21**(3), 04021010. https://doi.org/10.1061/(ASCE)GM.1943-5622.0001940.
Kou, M.M., Liu, X.R., Tang, S.D. and Wang, Y.T. (2019), "3-D X-ray computed tomography on failure characteristics of rock-like materials under coupled hydro-mechanical loading", *Theor. Appl. Fract. Mech.*, **104**, 102396. https://doi.org/10.1016/j.tafmec.2019.102396.
Lajtai, E.Z. (1974), "Brittle fracture in compression", *Int. J. Fract.*, **10**(4), 525-36. https://doi.org/10.1007/BF00155255.
Lee, H. and Jeon, S. (2011), "An experimental and numerical study of fracture coalescence in pre-cracked specimens under uniaxial compression", *Int. J. Solids Struct.*, **48**(6), 979-999. https://doi.org/10.1016/j.ijsolstr.2010.12.001.
Lee, J. and Hong, J.W. (2018), "Crack initiation and fragmentation processes in pre-cracked rock-like materials", *Geomech. Eng.*, **15**(5), 1047-1059. https://doi.org/10.12989/gae.2018.15.5.1047.
Liu, B.L., Yang, H. Q., Karekal, S. (2020) "Effect of water content on argillization of mudstone during the tunnelling process", *Rock Mech. Rock Eng.*, **53**(2), 799-813. https://doi.org/10.1007/s00603-019-01947-w.
Liu, X.W., Liu, Q.S., Liu, B., Zhu, Y.G. and Zhang, P.L. (2019) "Failure behavior for rock-like material with cross crack under biaxial compression", *J. Mater. Civ. Eng.*, **31**(2), 06018025. https://doi.org/10.1061/(ASCE)MT.1943-5533.0002540.
Lotidis, M.A., Nomikos, P.P. and Sofianos, A.I. (2019), "Numerical study of the fracturing process in marble and plaster hollow plate specimens subjected to uniaxial compression", *Rock Mech. Rock Eng.*, **52**(11), 4361-4386. https://doi.org/10.1007/s00603-019-01884-8.
Lv, H.Y., Tang, Y.S., Zhang, L.F., Cheng, Z.B. and Zhang, Y.N. (2019), "Analysis for mechanical characteristics and failure models of coal specimens with non-penetrating single crack", *Geomech. Eng.*, **17**(4), 355-365. https://doi.org/10.12989/gae.2019.17.4.355.
Manterola, J., Cabello, M., Zurbitu, J., Renart, J., Turon, A., Jumel, J. and Urresti, I. (2019), "Effect of the width-to-thickness ratio on the mode I fracture toughness of flexible bonded joints", *Eng. Fract. Mech.*, **218**, UNSP 106584. https://doi.org/10.1016/j.engfracmech.2019.106584.
Manouchehrian, A., Sharifzadeh, M. and Marji, M.F. and Gholamnejad J. (2014), "A bonded particle model for analysis of the flaw orientation effect on crack propagation mechanism in brittle materials under compression", *Arch. Civ. Mech. Eng.*, **14**(1), 40-52. https://doi.org/10.1016/j.acme.2013.05.008.
Park, C.H. and Bobet, A. (2010), "Crack initiation, propagation and coalescence from frictional flaws in uniaxial compression", *Eng. Fract. Mech.*, **77**(14), 2727-2748. https://doi.org/10.1016/j.engfracmech.2010.06.027.
Potyondy, D.O. and Cundall PA. (2004), "A bonded-particle model for rock", *Int. J. Rock Mech. Min. Sci.*, **41**(8),1329-1364. https://doi.org/10.1016/j.ijrmms.2004.09.011.
Petit, J. and Barquins, M. (1988), "Can natural faults propagate under mode II conditions", *Tectonics*, **7**(6), 1246-1265. https://doi.org/10.1029/TC007i006p01243.
Pizzati, M., Balsamo, F., Storti, F. and Iacumin, P. (2019), "Physical and chemical strain-hardening during faulting in poorly lithified sandstone: The role of kinematic stress field and selective cementation", *Geol. Soc. Amer. Bull.*, **132**(5-6), 1183-1200. https://doi.org/10.1130/B35296.1.
Pizzati, M., Balsamo, F. and Storti, F. (2020), "Displacement-dependent microstructural and petrophysical properties of deformation bands and gouges in poorly lithified sandstone deformed at shallow burial depth (Crotone Basin, Italy)", *J. Struct. Geol.*, **137**, 104069. https://doi.org/10.1016/j.jsg.2020.104069.
Sun, W.B., Du, H.Q., Zhou, F. and Shao, J.L. (2019), "Experimental study of crack propagation of rock-like specimens containing conjugate fractures", *Geomech. Eng.*, **17**(4), 323-331. https://doi.org/10.12989/gae.2019.17.4.323.
Shen, B. (1995), "The mechanism of fracture coalescence in compression-experimental-study and numerical-simulation", *Eng. Fract. Mech.*, **51**(1), 73-85. https://doi.org/10.1016/0013-7944(94)00201-R.
Sagong, M. and Bobet, A. (2002), "Coalescence of multiple flaws in a rock-model material in uniaxial compression", *Int. J. Rock Mech. Min. Sci.*, **39**(2), 229-241. https://doi.org/10.1016/S1365-1609(02)00027-8.
Scholtès, L. and Donzé, F. (2013), "A DEM model for soft and hard rocks: Role of grain interlocking on strength", *J. Mech. Phys. Solids*, **61**(2), 352-369. https://doi.org/10.1016/j.jmps.2012.10.005.
Song, Z.Y., Konietzky, H. and Herbst, M. (2019), "Three-dimensional particle model based numerical simulation on multi-level compressive cyclic loading of concrete", *Constr. Build. Mater.*, **225**, 661-677. https://doi.org/10.1016/j.conbuildmat.2019.07.260.
Tian, W.L. and Yang, S.Q. (2017), "Experimental and numerical study on the fracture coalescence behavior of rock-like materials containing two non-coplanar filled flaws under uniaxial compression", *Geomech. Eng.*, **12**(3), 541-560. https://doi.org/10.12989/gae.2017.12.3.541.
Wong, R.H.C., Chau, K.T., Tang, C.A. and Lin, P. (2001), "Analysis of crack coalescence in rock-like materials containing three flaws-part i: Experimental approach", *Int. J. Rock Mech. Min. Sci.*, **38**(7), 909-924. https://doi.org/10.1016/S1365-1609(01)00064-8.
Wong, L.N.Y. and Li, H.Q. (2013), "Numerical study on coalescence of two coplanar pre-existing flaws in rock", *Int. J. Solids Struct.*, **50**, 3685-3706. https://doi.org/10.1016/j.ijsolstr.2013.07.010.
Wang, D.J., Tang, H.M., Elsworth, D. and Wang, C.Y. (2019), "Fracture evolution in artificial bedded rocks containing a structural flaw under uniaxial compression", *Eng. Geol.*, **250**, 130-141. https://doi.org/10.1016/j.enggeo.2019.01.011.
Xiong, F., Jing, H.W., Su, H.J., Du, M.R., Yin, Q. and Han G.S. (2017), "Strength and fracture behaviors of sandstone samples containing intersect fissures under uniaxial compression", *J. China Coal Soc.*, **42**(4), 886-895 (in Chinese). https://doi.org/10.13225 /j.cnki.jccs.2016.1695.
Yang, S.Q., Huang, Y.H., Jing, H.W. and Liu, X.R. (2014), "Discrete element modeling on fracture coalescence behavior of red sandstone containing two unparallel flaws under uniaxial compression", *Eng. Geol.*, **178**, 28-48. https://doi.org/10.1016/j.enggeo.2014.06.005.
Yang, S.Q. and Jing, H.W. (2011), "Strength failure and crack coalescence behavior of brittle sandstone samples containing a single flaw under uniaxial compression", *Int. J. Fract.*, **168**(2), 227-250. https://doi.org/10.1007/s10704-010-9576-4.
Yin, Q., Jing, H.W. and Zhu, T.T. (2016), "Mechanical behavior and failure analysis of granite specimens containing two orthogonal flaws under uniaxial compression", *Arab. J. Geosci.*, **9**(1), 31. https://doi.org/10.1007/s12517-015-2078-y.
Yi, J.T., Liu, F., Zhang, T.B., Qiu, Z.Z. and Zhang, X.Y. (2021), "Determination of the ultimate consolidation settlement of jack-up spudcan footings embedded in clays", *Ocean Eng.*, **236**, 109509. https://doi.org/10.1016/j.oceaneng.2021.109509.
Zhang, X.P. and Wong, L.N.Y. (2012), "Cracking processes in

rock-like material containing a single flaw under uniaxial compression: a numerical study based on parallel bonded-particle model approach", *Rock Mech. Rock Eng.*, **45**(5), 711-737. https://doi.org/10.1007/s00603-011-0176-z.

Zhang, X.P. and Wong, L.N.Y. (2013), "Loading rate effects on cracking behavior of flaw-contained specimens under uniaxial compression", *Int. J. Fract.*, **180**, 93-110. https://doi.org/10.1007/s10704-012-9803-2.

Zhang, X.P. and Wong, L.N.Y. (2014), "Displacement field analysis for cracking processes in bonded-particle model", *B. Eng. Geol. Environ.*, **73**(1), 13-21. https://doi.org/10.1007/s10064-013-0496-1

Zeng, W., Yang, S.Q. and Tian, W.L. (2018), "Experimental and numerical investigation of brittle sandstone specimens containing different shapes of holes under uniaxial compression", *Eng. Fract. Mech.*, **200**, 430-450. https://doi.org/10.1016/j.engfracmech.2018.08.016.

Zhao, C., Zhou, Y.M., Zhao, C.F. and Bao, C. (2018), "Cracking processes and coalescence modes in rock-like specimens with two parallel pre-existing cracks", *Rock Mech. Rock Eng.*, **51**(11), 3377-3393. https://doi.org/10.1007/s00603-018-1525-y.

Zhang, B., Li, S.C., Yang, X.Y., Xia, K.W., Liu, J.Y., Guo, S. and Wang, S.G. (2019), "The coalescence and strength of rock-like materials containing two aligned X-type flaws under uniaxial compression", *Geomech. Eng.*, **17**(1), 47-56. https://doi.org/ 10.12989/gae.2019.17.1.047.

Zhou, Y., Zhao, D.J., Li, B., Wang, H.Y., Tang Q.Q. and Zhang, Z.Z. (2021), "Fatigue damage mechanism and deformation behaviour of granite under ultrahigh-frequency cyclic loading conditions", *Rock Mech. Rock Eng.*, **54**, 4723-4739. https://doi.org/10.1007/s00603-021-02524-w.

*CC*